NASA/TM–20240000817

Application of PLIF to Investigate the Hypersonic Wake of a LOFTID-Relevant Model at Mach 10

Neil S. Rodrigues, Olivia K. Tyrrell, Paul M. Danehy, Elizabeth F. Rieken, Brian R. Hollis, William H. Ripley and Jonathan B. Crider
Langley Research Center, Hampton, Virginia

Anthony W. Robbins, Tina Reynolds, and Sheila A. Wright
Jacobs Technology Inc., Hampton, Virginia

April 2024

NASA STI Program Report Series

Since its founding, NASA has been dedicated to the advancement of aeronautics and space science. The NASA scientific and technical information (STI) program plays a key part in helping NASA maintain this important role.

The NASA STI program operates under the auspices of the Agency Chief Information Officer. It collects, organizes, provides for archiving, and disseminates NASA's STI. The NASA STI program provides access to the NTRS Registered and its public interface, the NASA Technical Reports Server, thus providing one of the largest collections of aeronautical and space science STI in the world. Results are published in both non-NASA channels and by NASA in the NASA STI Report Series, which includes the following report types:

- TECHNICAL PUBLICATION. Reports of completed research or a major significant phase of research that present the results of NASA Programs and include extensive data or theoretical analysis. Includes compilations of significant scientific and technical data and information deemed to be of continuing reference value. NASA counterpart of peer-reviewed formal professional papers but has less stringent limitations on manuscript length and extent of graphic presentations.

- TECHNICAL MEMORANDUM. Scientific and technical findings that are preliminary or of specialized interest, e.g., quick release reports, working papers, and bibliographies that contain minimal annotation. Does not contain extensive analysis.

- CONTRACTOR REPORT. Scientific and technical findings by NASA-sponsored contractors and grantees.

- CONFERENCE PUBLICATION. Collected papers from scientific and technical conferences, symposia, seminars, or other meetings sponsored or co-sponsored by NASA.

- SPECIAL PUBLICATION. Scientific, technical, or historical information from NASA programs, projects, and missions, often concerned with subjects having substantial public interest.

- TECHNICAL TRANSLATION. English-language translations of foreign scientific and technical material pertinent to NASA's mission.

Specialized services also include organizing and publishing research results, distributing specialized research announcements and feeds, providing information desk and personal search support, and enabling data exchange services.

For more information about the NASA STI program, see the following:

- Access the NASA STI program home page at http://www.sti.nasa.gov

- Help desk contact information:

https://www.sti.nasa.gov/sti-contact-form/
and select the "General" help request type.

NASA/TM–20240000817

Application of PLIF to Investigate the Hypersonic Wake of a LOFTID-Relevant Model at Mach 10

Neil S. Rodrigues, Olivia K. Tyrrell, Paul M. Danehy, Elizabeth F. Rieken, Brian R. Hollis, William H. Ripley, and Jonathan B. Crider
Langley Research Center, Hampton, Virginia

Anthony W. Robbins, Tina Reynolds, and Sheila A. Wright
Jacobs Technology Inc., Hampton, Virginia

National Aeronautics and
Space Administration

Langley Research Center
Hampton, Virginia 23681-2199

April 2024

Available from:

NASA STI Program / Mail Stop 050
NASA Langley Research Center
Hampton, VA 23681-2199

Table of Contents

List of Figures

Abstract

An experimental investigation of hypersonic wake flows using the planar laser-induced fluorescence (PLIF) measurement technique is summarized in this report. Off-body measurements, primarily flow visualization and velocity, were obtained for the wake of a blunt body model relevant for terrestrial re-entry and Martian entry applications within a Mach 10 hypersonic flow. The design of the model was based on the forebody aeroshell used for the LOFTID (Low-Earth Orbit Flight Test of an Inflatable Decelerator) flight vehicle. This document serves to document the experimental set-up, test conditions, and initial data analysis of select test conditions.

Nomenclature

Symbols

P	pressure
Re/L	unit Reynolds number
T	temperature
α	model angle of attack
φ	model roll angle

Subscripts and Superscripts

∞	wind tunnel free stream condition
0	wind tunnel stagnation or reservoir condition

Acronyms

FV	flow visualization
LAL	Langley aerothermodynamics laboratory
LFS	laser frequency scan
LTI	lifetime imaging
MTV	molecular tagging velocimetry
NO	nitric oxide
PLIF	planar laser-induced fluorescence
SLA	stereolithography
SLM	standard liter per minute
TI	temperature imaging

Introduction

This report serves to document an experimental dataset of hypersonic wake flow measurements obtained at the NASA Langley 31-inch Mach 10 Air Tunnel in November 2022. Off-body measurements were obtained of a blunt body model relevant for terrestrial re-entry and Martian entry applications. The design of the model was based on the aeroshell used for the LOFTID (Low-Earth Orbit Flight Test of an Inflatable Decelerator) flight vehicle (Swanson, *et al.*, 2019). Unlike the LOFTID model, which had a toroidal shaped back-shell, a smooth back-shell was used for all runs with this test entry, with 130 small holes located on the aft-body to seed the wake flow with nitric oxide (NO) gas. The seeding enabled two-dimensional (2D) planar visualizations of the wake using planar laser-induced fluorescence (PLIF), which is a spatially resolved (<1 mm) and temporally resolved (<1 μs) laser-based measurement technique. This document serves to summarize the experimental conditions and provide an initial analysis of select test conditions.

Background

Wind tunnel measurements often rely on nonintrusive, laser-based measurement techniques for flow visualization, velocity, and temperature measurements. Planar laser-induced fluorescence (PLIF) using the NO molecule has been widely used in wind tunnel facilities (Danehy *et al.*, 2018). NO is either premixed with the wind tunnel test gas, locally injected, or naturally present, for example in arc-heated and shock-heated facilities, including shock tubes or shock tunnels. NO-PLIF experiments have typically been performed within the A-X electronic system, with the majority of studies using ($v' = 0$, $v'' = 0$) excitation near 226 nm. The reader is directed to references such as Eckbreth (1996) for a more thorough background on the PLIF measurement technique.

Experimental Systems

Wind Tunnel Test Facility

All measurements were obtained at the 31-inch Mach 10 Air Tunnel located at the Langley Aerothermodynamics Laboratory (LAL), at the NASA Langley Research Center. Detailed information on the 31-in Mach 10 Air Tunnel can be found in Berger *et al.* (2015). Figure 1 provides a schematic of the 31-in Mach 10 Air Tunnel, courtesy of Richard A. Wheless from the NASA Langley Research Center. The test data described in this report was obtained during an entry labeled as *Test 548* by the wind tunnel facility.

Wind Tunnel Model

The wind tunnel model used for this work was a 70-degree sphere-cone that was designed based on the LOFTID (Low-Earth Orbit Flight Test of an Inflatable Decelerator) flight vehicle. The model featured a metal forebody, with an outer diameter of 5", and a stereolithography (SLA) manufactured plastic aft body. An internal gas pathway design allowed nitric oxide (NO) to flow into the model through a small tube and seed the wake through 130 small holes located on the aft body. The small (0.022"-0.044" diameter) holes were located in a pattern designed with the intention of promoting uniform seeding. Additional details on the model can be found in a *Model Systems Report* (Cagle, 2021). A smooth aft-body design was used for this test entry and the *blade* sting was used to hold the model within the wind tunnel for this test. A CAD

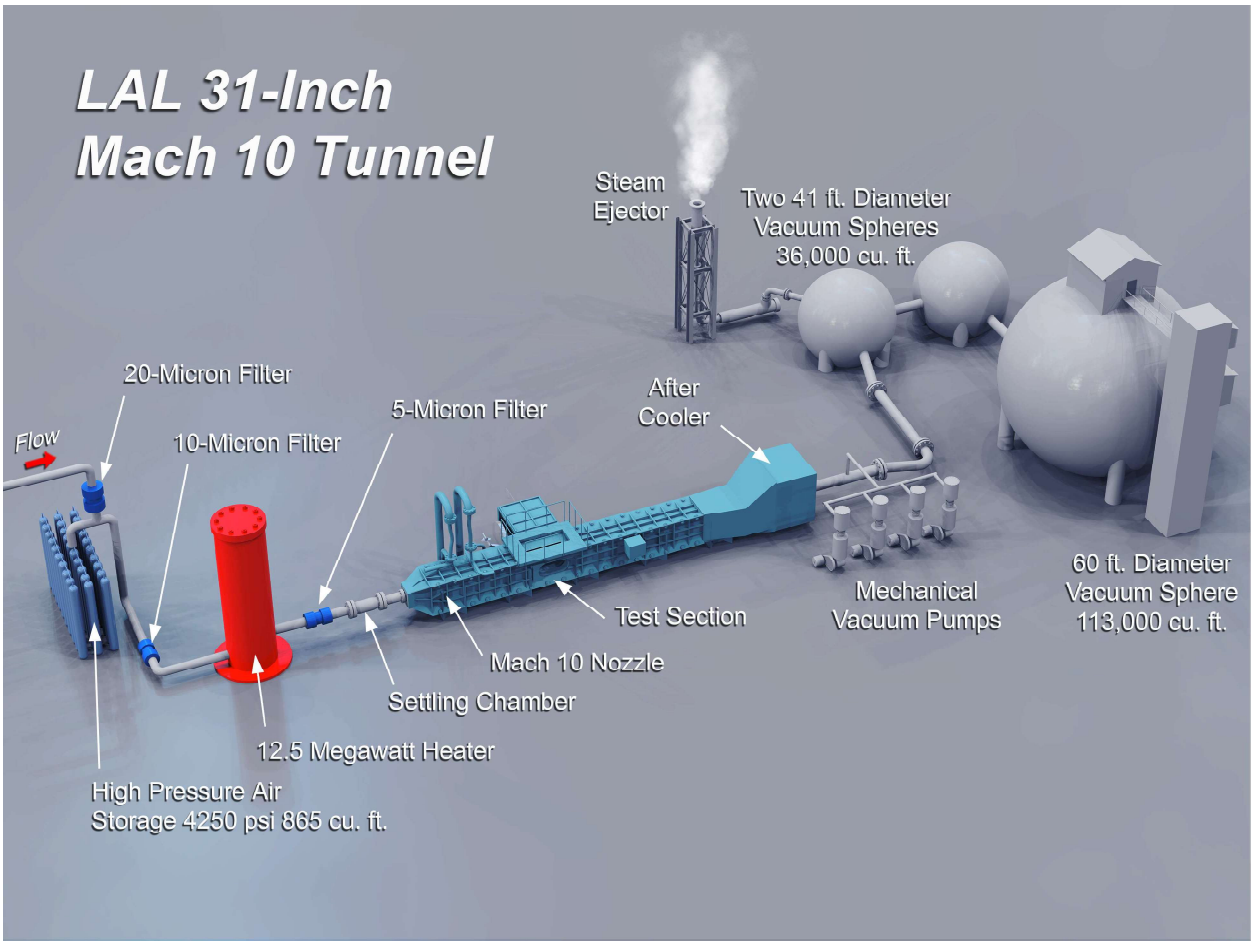

Figure 1. 3D schematic of the Langley Aerothermodynamics Laboratory (LAL) 31-inch Mach 10 Air Tunnel, courtesy of Richard A. Wheless from the NASA Langley Research Center.

schematic of the wind tunnel model is shown in Fig. 2. A *straight* sting was also manufactured but was not used for this test entry.

Planar Laser-Induced Fluorescence (PLIF) System

The planar laser-induced fluorescence (PLIF) system used for this work consisted of a laser, sheet forming optics, and two cameras located adjacent to the wind tunnel. The laser was a 10-ns pulsed Spectra Physics® Pro-230 Nd:YAG laser operating at a 10 Hz repetition-rate that was used to pump a Sirah® Cobra Stretch dye laser at 532-nm to generate a 622-nm output beam. This output was mixed with 355-nm light from the Nd:YAG in a Sirah Frequency Conversion Unit (FCU) to produce ~3.5 mJ per pulse of tunable ultraviolet (UV) light near 226-nm. The laser was tuned to different absorption lines in the A-X(0,0) band of nitric oxide. Figure 3 shows a schematic representation of the laser system, which was located in an enclosed cart and placed near the downstream side of the wind tunnel. This laser beam was directed with mirrors to the sheet-forming optics located above the tunnel test section as shown in Fig. 4. A series of mirrors and optics placed on motorized stages directed the laser downward towards large UV-transmissive windows. Figure 5(a) schematically shows the formation of the laser beam into a laser sheet for flow visualization: the collimated 226-nm laser beam was passed through a 20-mm focal length concave cylindrical lens that diverged the beam in the streamwise direction, expanding it to about 152 mm (6") in that dimension. A 152 mm (6") diameter 1-meter focal length convex spherical lens with a clear aperture

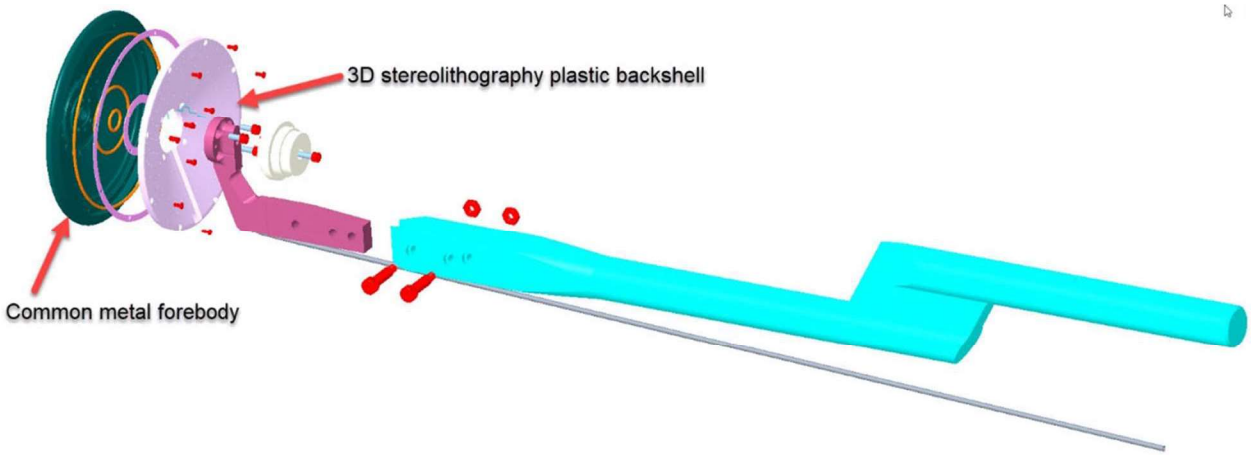

Figure 2. 3D schematic of the wake flow model used for the present work, which is referred to as the *LOFTID-relevant, smooth-blade* model due to its 70-degree forebody, smooth aft-body, and blade-style sting. Discrete holes are located on the aft body to facilitate the seeding of the nitric oxide (NO) gas. The model was designed by C. Mark Cagle from the NASA Langley Research Center.

of approximately 140 mm (5.5") diameter was used to collimate the beam in the streamwise direction, while focusing the beam into a thin sheet in the transverse direction. To perform molecular tagging velocimetry, the cylindrical lens was replaced by a commercial 1D diffractive optical element. As shown in Fig. 5(b), the collimated 226-nm laser beam was split into 75 laser beams of nearly equal laser intensity. The same 1-meter focal length lens collimated the diverging angles of these beams while simultaneously focusing each individual beam at the centerline of the tunnel. Fluorescence from these laser beams are viewed as parallel lines by the camera, located on the side window of the tunnel in Fig. 4. Each of these lines tag NO seeded into the flow to measure velocity using the method identical to the one used by Bathel *et al.* (2011). However, compared to the previous work, three times as many laser beams are generated by the current

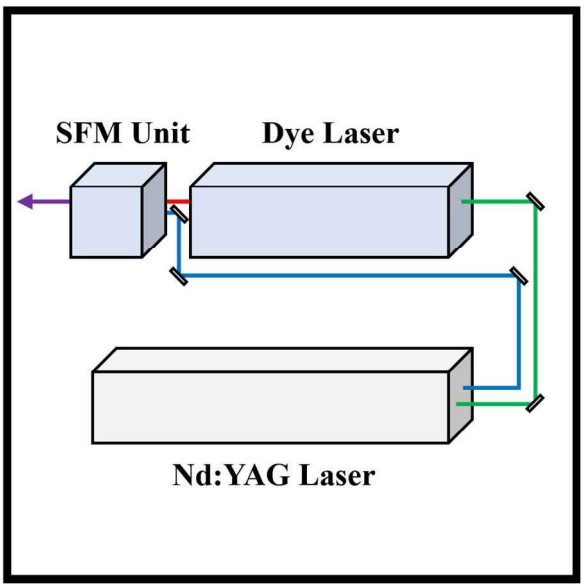

Figure 3. Schematic diagrams of the PLIF laser system featuring the Nd:YAG pump and dye laser system used to generate 226-nm tunable light. The PLIF laser system was placed within an enclosed cart and located near the downstream side of the wind tunnel.

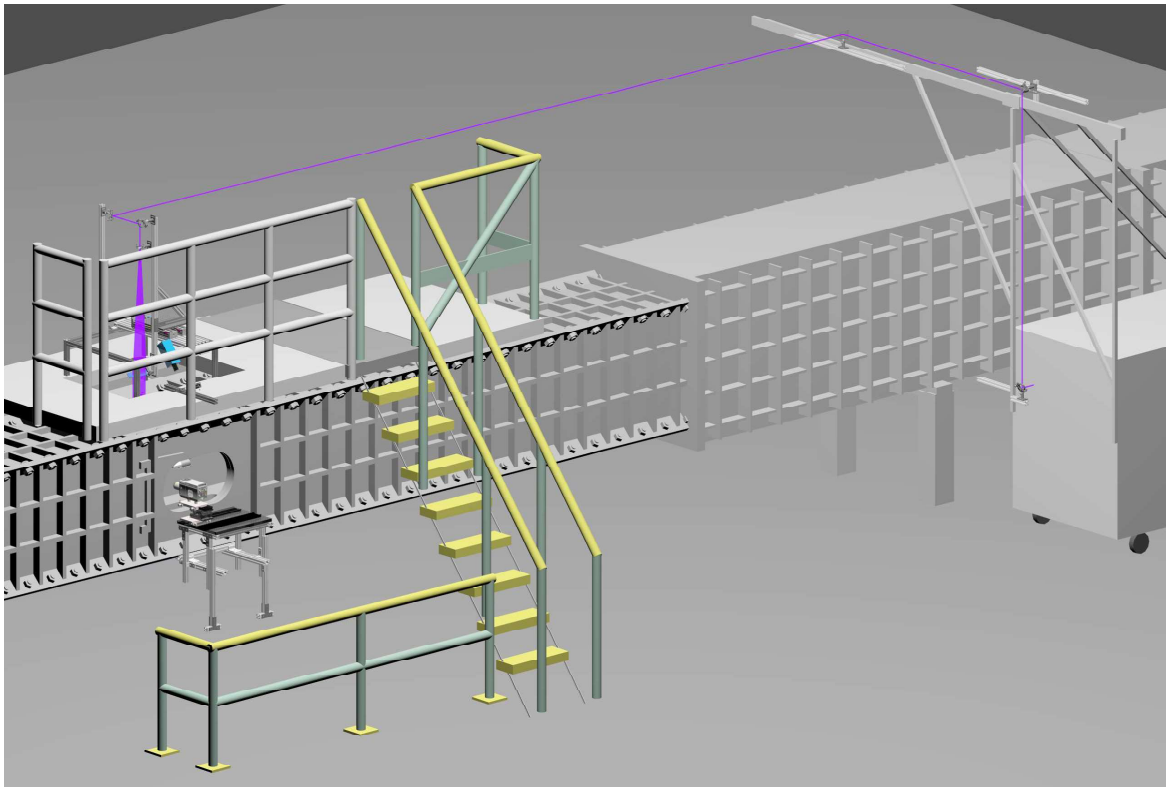

Figure 4. CAD schematic of laser propagation at the 31-in Mach 10 facility from the enclosed cart housing the PLIF laser systems to the test section of the wind tunnel.

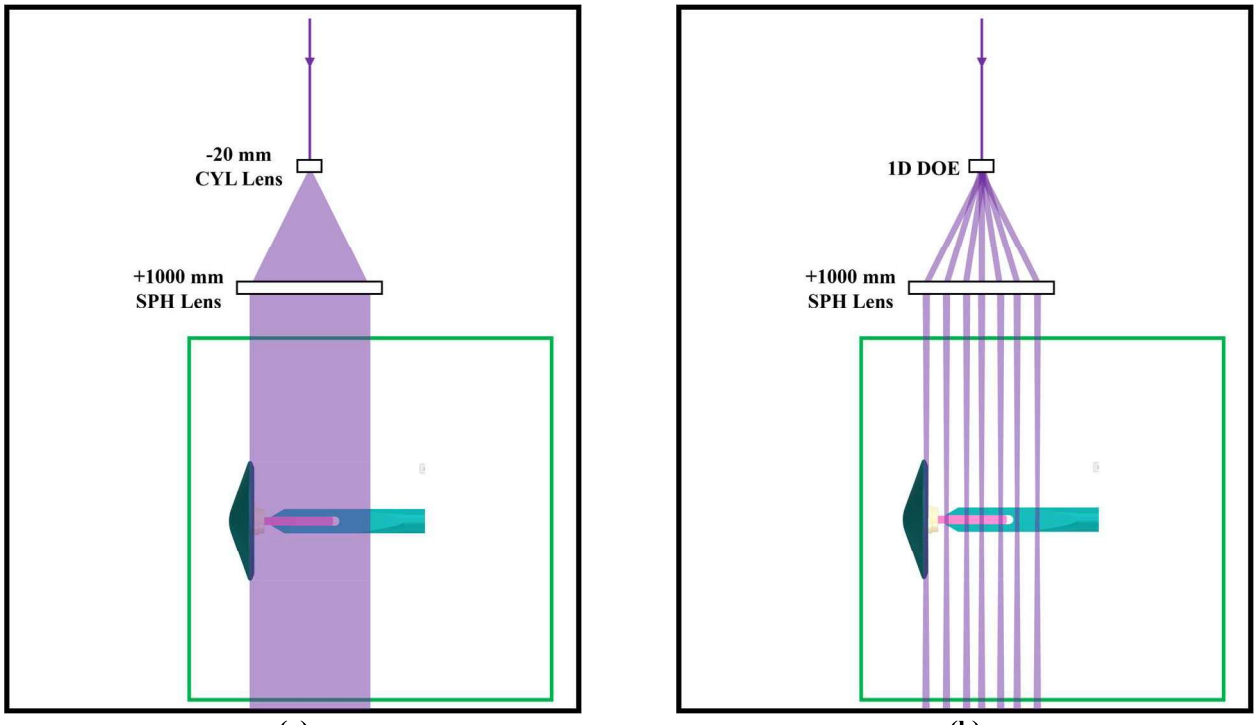

(a) **(b)**

Figure 5. Laser optics installed near the test section (represented by the green block) to generate the: (a) laser sheet for PLIF flow visualization, (b) PLIF molecular tagging velocimetry (MTV).

method (75 vs. 25). In addition, the current method is believed to produce narrower beams.

The primary PLIF camera system consisted of an intensified Andor® iStar front-illuminated scientific CMOS (sCMOS) camera operated with two different lenses to obtain different fields of view with different corresponding spatial resolutions. The camera sensor had 2560 by 2160 pixels, each having a 6.5-micron pixel size. The camera had an 18-mm diameter WE-AGT photocathode with ultra-fast gating and used the P46 phosphor. Most of the PLIF images were acquired with a 45-mm focal length *f*/1.8 UV lens, which provided a field-of-view large enough to view the entire vertical wake across the vehicle's diameter. Some images were obtained with a longer 100-mm focal length, *f*/2.8 lens, which provided higher spatial resolution over a smaller field-of-view. A UV transmissive glass plate was used as a beam-splitter immediately before the top window of the wind tunnel to direct ~1% of the laser sheet energy to a BK7 diffuser plate. Blue fluorescence emitted by the glass diffuser was captured by a Cooke® SensiCam CCD for every laser pulse to provide a shot-to-shot correction of the variation in laser intensity across the laser sheet.

Figure 6 shows CAD schematics of the PLIF experimental set-up at the test section: wind tunnel model at the centerline, laser sheet entering through the top window and exiting through the bottom window, PLIF camera located at the side window of tunnel and laser sheet profiling camera located at top window. Three different model orientations were used for this test entry, with the majority of the test runs occurring with the angle of attack $\alpha = 0°$ and model roll angle $\varphi = 0°$, as shown schematically in Fig. 7(a). Two alternative configurations were also used: $\alpha = -5°$ and $\varphi = 0°$ as shown schematically in Fig. 7(b) and $\alpha = 0°$ and $\varphi = 90°$ as shown schematically in Fig. 7(c). The view of the PLIF camera was designed such that all three model positions could be adequately covered without moving the position of the physical camera. The simulated camera views with the 45 mm camera lens for each of these three configurations are shown in Fig. 8 and the corresponding actual view from the PLIF camera, operating in long-exposure mode, is shown in Fig. 9. Both designed and actual views with the 100-mm focal length camera lens are shown in Fig. 10.

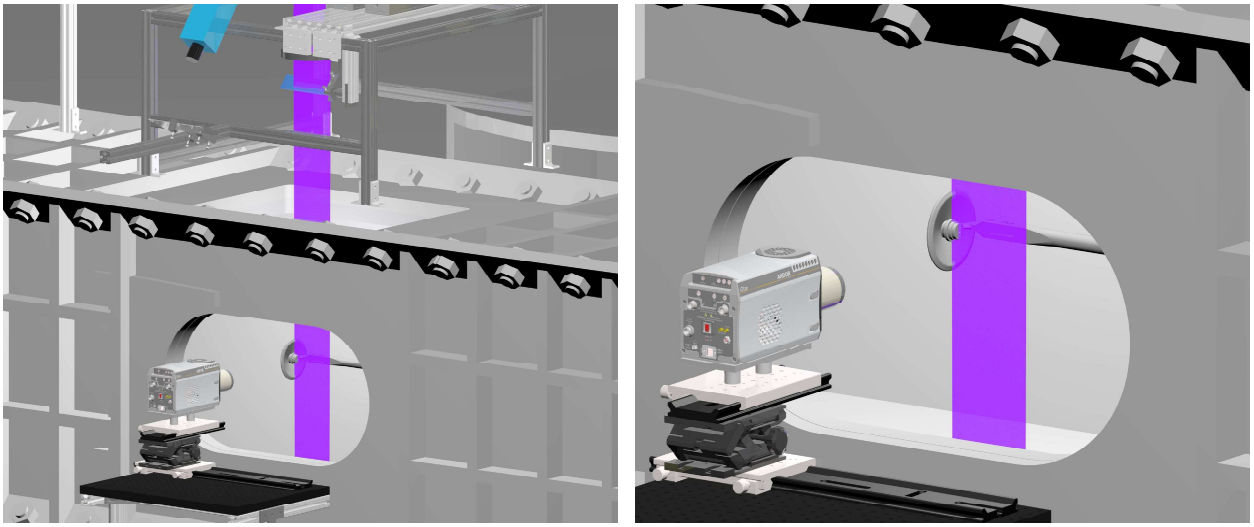

(a) **(b)**

Figure 6. CAD schematics of PLIF experimental set-up at test section: (a) view showing laser sheet propagating from top window of tunnel, (b) view showing PLIF camera mounted near side window of tunnel.

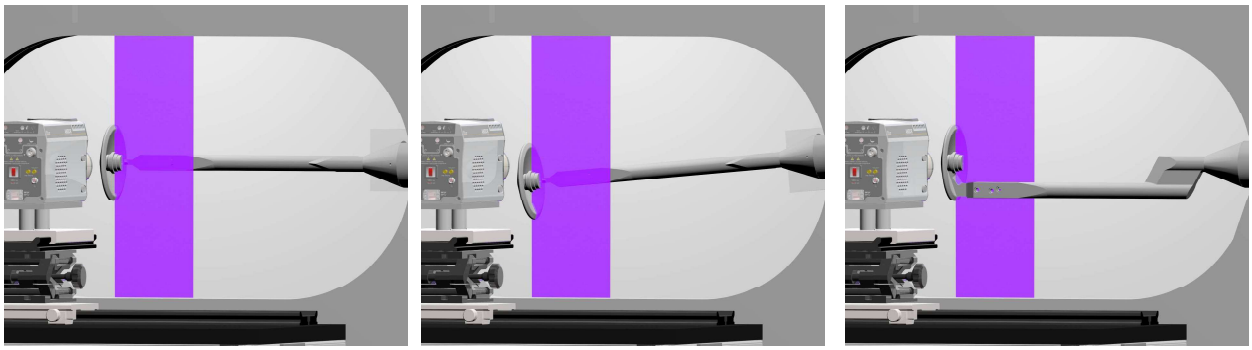

(a) (b) (c)

Figure 7. CAD schematics showing model orientations for three different configurations of angle of attack (α) and model roll (φ) : (a) α = 0°, φ = 0°, (b) α = -5°, φ = 0°, (c) α = 0°, φ = 90°.

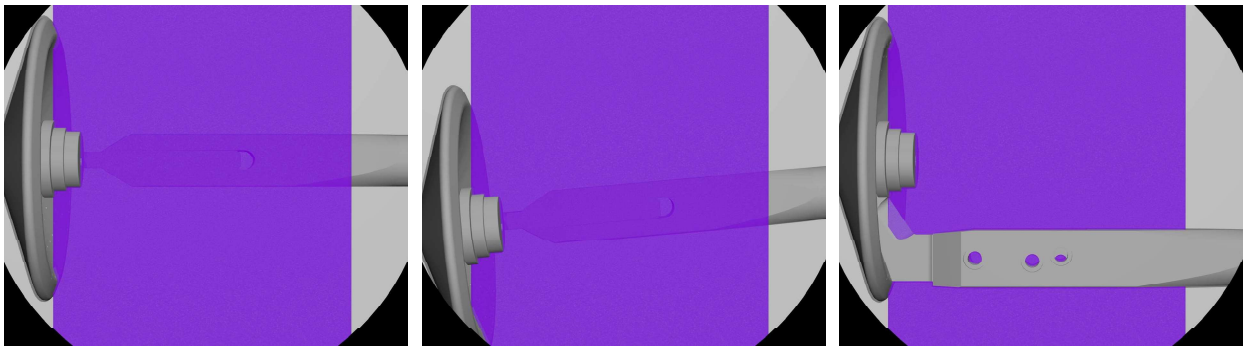

(a) (b) (c)

Figure 8. CAD schematics showing designed view from the PLIF camera (equipped with a 45-mm UV lens) for the three model configurations: (a) α = 0°, φ = 0°, (b) α = -5°, φ = 0°, (c) α = 0°, φ = 90°.

Figure 9. View from the PLIF camera (equipped with a 45 mm UV lens) in long-exposure mode for the three model configurations: (a) α = 0°, β = 0°, (a) α = -5°, β = 0°, (a) α = 0°, β = 90°.

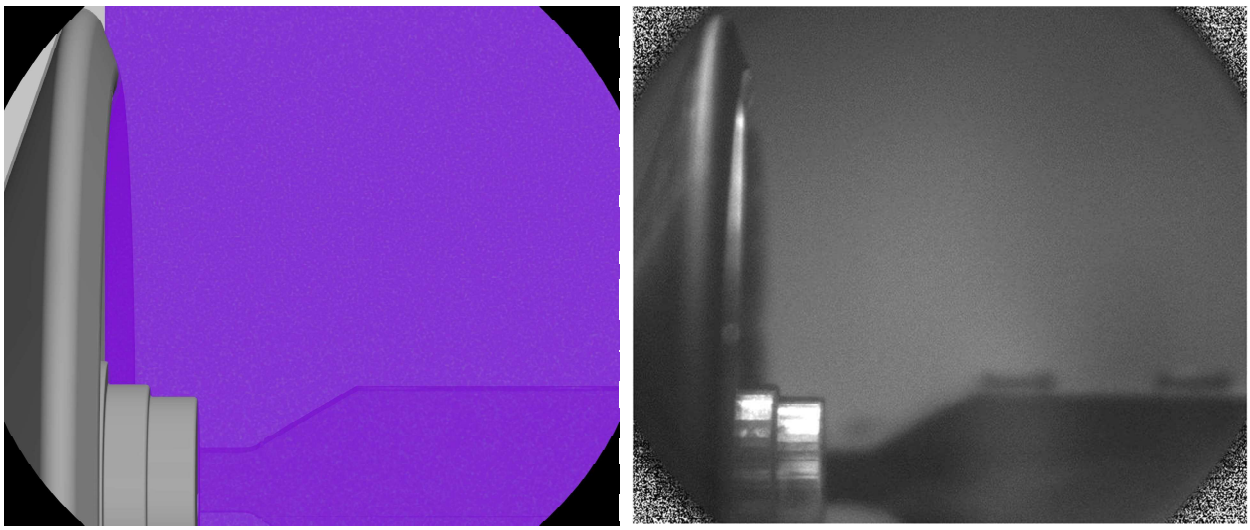

(a) (b)

Figure 10. (a) CAD schematic showing designed view and (b) view from the PLIF camera in long-exposure mode for the configuration with the 100-mm UV lens for (a) $\alpha = 0°$, $\varphi = 0°$.

Virtual Diagnostics Interface (ViDI) Procedure

To visualize the post-processed experimental data, the 2D PLIF image planes, which were acquired at the centerline of the test section, were imported into Autodesk 3ds Max and used to visualize the data using aspects of the Virtual Diagnostics Interface (ViDI). ViDI, which has been described by Schwartz and Fleming (2007), contains a virtual environment of the experimental facility and setup of the optical diagnostics system, including the camera system. The 2D image plane containing the PLIF image can be overlaid onto a CAD version of the test article, thereby ensuring that the scale and placement of the image match the dimensions of the model. A virtual camera can be placed within the environment to match the position of the physical camera used in the experiment. Simulated camera views can be rendered to match the field-of-view of the experimental data, with the 3D model of the test article and the 2D PLIF images overlaid together. This process can be useful to orient the PLIF intensity field and other off-body measurements to the wind tunnel model.

Test Campaign Overview

A detailed list of runs for the test campaign is provided in Table 1. Run 1 was a wind-off run to verify synchronization and proper operation of all systems, including: model injection, facility data acquisition, timing synchronization between the laser and cameras, triggering of the cameras, and operation of the nitric oxide (NO) mass flow meter. In total, 46 wind-on runs were performed as part of the test campaign. Data from 12 of those runs appear in this report and are denoted in bold text within the table.

Runs 2-15 are designated as shakedown runs for the model (this was the first test entry for this model) and for the PLIF measurement technique. Specific aspects of the PLIF that required shakedown included determining the needed levels of NO gas for seeding and optimizing the camera gain for high signal-to-noise ratios and high dynamic range. Twelve of these runs were performed at the three "standard" facility operating conditions near $Re_\infty/L = 0.5 \cdot 10^6$ ft^{-1}, $1.0 \cdot 10^6$ ft^{-1}, and $1.8 \cdot 10^6$ ft^{-1} and with the baseline geometric condition of angle of attack $\alpha = 0°$ and roll angle $\varphi = 0°$ for the model. Unsteady wake behavior was observed at all three standard conditions based on the flow visualization images, although increased levels of general unsteadiness could be observed with increasing Reynolds numbers. Two different hole diameters of 0.022" and 0.030" were used for these shakedown tests. PLIF flow visualization appeared to be very

similar for both hole diameters. One run was performed near $Re_\infty/L = 0.25 \cdot 10^6$ ft^{-1} to see if steady laminar behavior could be observed within the operating envelop of the facility for this geometry; unsteady behavior was also observed here. A run was performed with the model rolled to $\varphi = 90°$ in order to observe sting effects. During this run, some jet-in-crossflow-like flow structures were observed to be emanating from a gap on the model sting. This gap can be clearly seen within the CAD rendering of the model shown in Figs 8(b) and 8(c). Facility technicians used high-temperature tape to cover this gap in the sting and this geometry change is denoted with the bold vertical line between run 15 and 16. Sealing this gap eliminated the jet-like flow structures in subsequent runs.

Runs 16-19 were performed with the minimal amount of NO gas needed for adequate signal-to-noise images (0.05 SLM) for the purposes of flow visualization. One run was performed at each of the three standard test conditions for roll angle $\beta = 0°$ and one run was performed for $\beta = 90°$ at the low Reynolds number condition. The three $\beta = 0°$ runs at the NO flow rate of 0.05 SLM can be directly compared with three later runs at identical conditions performed with an NO flow rate of 1.00 SLM (run 30, 31, and 33). The 1.00 SLM was determined to be an acceptable amount of NO based on the shakedown test of the MTV (molecular tagging velocimetry) variant of PLIF, which was performed during runs 20-25. MTV runs for the planned test matrix were performed during runs 26-29 at the 1.00 SLM for the three standard conditions. At the low Reynolds number condition, the model angle of attack was changed to $\alpha = -5°$ in runs 29 and 32. The flow visualization runs 30-34 were also obtained at conditions identical to the MTV runs 26-29.

Runs 34-37 were performed using a variation of PLIF known as laser frequency scanning (denoted here with the LFS acronym). With this approach, the laser wavelength was programmed to change in picometer-level increments during the run to scan the laser wavelength over a PLIF absorption transition. Different absorption transitions (which are denoted in Table 1) were targeted for these measurements, compared to the Q-branch band-head used for the flow visualization and MTV runs. The $P_{12}(3.5)$ transition was used for runs at each of the three standard Reynolds numbers of the facility and an additional run was performed at the low Reynolds number using the $R_2(13.5)$ transition. The primary motivation for these runs was to attempt to measure the spanwise velocity using the Doppler shift of the absorption transition peak. The $P_{12}(3.5)$ and $R_2(13.5)$ transitions were specifically chosen due to the non-overlapping features of these transitions and their similar Einstein B coefficient. Data from both runs at the low Reynolds number condition using the $P_{12}(3.5)$ and $R_2(13.5)$ transitions (runs 36 and 37, respectively) could potentially be used to measure a rotational temperature. Thermometry may be performed using the LFS method, but an alternative temperature measurement approach of tuning the laser to the line center of these transitions was also performed at the low Reynolds number condition during runs 38 and 39.

The camera lens was changed from 45-mm to 100-mm focal length between runs 39 and 40. This changed the field-of-view from the entire span of the model and width of the laser sheet (obtained using the 45-mm lens) to a zoomed-in view using the 100-mm lens focusing on the top half of the model, with the camera as close to the test section window as possible. This allowed for the best possible spatial resolution, considering the limitations imposed by the size of the test section and commercially available ultraviolet-transmissive camera lenses. The improved spatial resolution was motivated by reducing the experimental uncertainty of the streamwise velocity data generated using MTV. Runs 40-43, which were obtained at the three typical Reynolds number conditions for $\alpha = 0°$ and at the low Reynolds number condition for $\alpha = -5°$, were performed as MTV runs to pair with the data acquired earlier with the 45-mm focal length lens. Additional variants of PLIF were attempted for Runs 44-47 to close out the test campaign. Run 44 used the same camera timing scheme as the molecular tagging velocimetry but with the laser sheet rather than laser lines was used to measure the lifetime of the NO fluorescence. Runs 45-47 combined the MTV and the LFS approach in order to attempt both streamwise and spanwise velocity measurements in a single run. Run 45 served as a shakedown run for this effort and was performed using a hole size of 0.044" due to the 0.022" not being available at the time of the test run.

Table 1. 31-Inch Mach 10 Air Tunnel Test 548 run matrix. Data from 12 runs are presented in this report and these runs are denoted in bold text.

Run #	Hole ⌀	$\dot{m}_{NO}$	α	φ	P_0	T_0	$Re_x/L \cdot 10^6$		Run	PLIF	PLIF	Camera
	(in.)	(SLM)	(°)	(°)	(psi)	(F)	(1/ft)	(1/m)	ID	Variant	Transition	Lens
1	*Wind-off check for all systems including injection, facility DAQ, laser/camera timing & trigger, NO flowmeter*											
2	0.030	0.5	0	0	722	1269	1.10	3.61	121	FV	Q_1(1.5)	45 mm
3		0.50		0	351	1277	0.55	1.80	111			
4		0.25		0	351	1275	0.55	1.80	112			
5		0.50		0	1305	1291	1.89	6.20	131			
6		1.00		0	722	1278	1.09	3.57	122			
7		0.50		0	152	1210	0.26	0.85	141			
8		0.50		90	351	1282	0.54	1.77	151			
9		*varied*		0	351	1283	0.54	1.77	113			
10		*varied*		0	722	1279	1.09	3.57	123			
11	0.022	0.05	0	0	722	1277	1.09	3.57	171	FV	Q_1(1.5)	
12		0.05			351	1278	0.55	1.80	161			
13		0.05			350	1279	0.55	1.80	162			
14		0.05			721	1280	1.09	3.57	172			
15		0.05			1306	1286	1.90	6.23	181			
16	0.022	0.05	0	0	721	1281	1.08	3.54	173	FV	Q_1(1.5)	
17		0.05		0	351	1279	0.55	1.80	163			
18		0.05		90	351	1281	0.54	1.77	191			
19		0.05		0	1305	1285	1.90	6.23	182			
20	0.030	0.10	0	0	722	1270	1.10	3.61	221	MTV	Q_1(1.5)	
21		0.10			350	1279	0.55	1.80	211			
22		0.40			722	1276	1.09	3.57	222			
23		0.80			351	1277	0.55	1.80	212			
24		1.00			350	1280	0.54	1.77	213			
25		1.00			1303	1280	1.91	6.26	231			
26	0.022	1.00	0	0	721	1277	1.09	3.57	271	MTV	Q_1(1.5)	
27			0		1303	1283	1.90	6.23	281			
29			0		350	1279	0.55	1.80	261			
29			-5		350	1279	0.54	1.77	262			
30	0.022	1.00	0	0	721	1277	1.09	3.57	174	FV	Q_1(1.5)	
31			0		350	1279	0.54	1.77	164			
32			-5		350	1279	0.54	1.77	165			
33			0		1305	1271	1.93	6.33	183			
34	0.022	1.00	0	0	721	1275	1.09	3.57	371	LFS	P_{12}(3.5)	
35					1304	1274	1.92	6.30	381			
36					350	1280	0.54	1.77	361			
37					350	1279	0.54	1.77	362		R_2(13.5)	
38	0.022	1.00	0	0	350	1279	0.54	1.77	461	TI	P_{12}(3.5)	
39					350	1280	0.54	1.77	462		R_2(13.5)	
40	0.022	1.00	0	0	721	1278	1.09	3.57	571	MTV	Q_1(1.5)	100 mm
41					350	1278	0.54	1.77	561			
42					1304	1275	1.92	6.30	581			
43					351	1278	0.55	1.80	562			
44	0.022	1.00	0	0	1305	1271	1.93	6.33	661	LTI	Q_1(1.5)	
45	0.044	1.00	0	0	351	1278	0.55	1.80	761	MTV + LFS	P_{12}(3.5)	
46	0.022				350	1278	0.55	1.80	563		P_{12}(3.5)	
47					350	1280	0.54	1.77	564		R_2(13.5)	

Experimental Results

An illustration of the data processing steps for the PLIF flow visualization is shown in Fig. 11 using an average PLIF image. The dark noise from the camera sensor and other camera artifacts are first subtracted by taking an average background of 5 images acquired immediately prior to the model being injected into the tunnel. The raw PLIF image is shown in Fig. 11(a) and the PLIF image after background subtraction is shown in Fig. 11(b). Other camera artifacts, such as an observed hexagonal pattern caused by the camera intensifier, are then removed using a flatfield correction, as shown in Fig. 11(c). The image is spatially calibrated, as shown in Fig. 11(d), with a dot card image using an in-house de-warping routine developed by Dr. Timothy Fahringer from the NASA Langley Research Center. The image is then corrected in the horizontal direction for the variation in intensity of the laser sheet, which is shown in Fig. 11(e). The origin of the spatial coordinates are then aligned to the model payload, as shown in Fig. 11(f), based on the edges of the intensity field and light scattered at the model surface near the payload.

Instantaneous PLIF images, rendered in false color and depicted using the ViDI platform, are shown in Fig. 12 for the angle of attack $\alpha = 0°$ and $\alpha = -5°$ configurations. For these images, a model roll angle $\varphi = 0°$, unit Reynolds number $Re_x/L = 0.54 \cdot 10^6$ ft^{-1}, and nitric oxide seed gas flow rate of 1.0 SLM were used. Instantaneous PLIF images are shown in Fig. 13 for the model roll angle $\varphi = 0°$ and $\beta = 90°$ configurations. These images correspond to $\alpha = 0°$, $Re_x/L = 0.54 \cdot 10^6$ ft^{-1}, and a nitric oxide seed gas flow rate of 0.05 SLM. Figure 14 shows a dual-orthogonal-plane reconstruction of the $\beta = 0°$ and $\beta = 90°$ average PLIF images oriented with respect to the model.

Time averaged PLIF images for the three standard Reynolds numbers and NO flow rates corresponding to 0.05 SLM and 1.00 SLM are shown in Fig. 15. Varying the NO flow rate by a factor of 20 appears to produce only very minimal changes in the shape and structure of the visualized wake. Since 0.05 SLM was determined to be the lowest level of NO gas seeding needed to visualize the wake, we believe that up to a mass flow rate of at least 1 SLM, the NO seed gas flow does not perturb the wake. A custom edge tracking algorithm was developed to determine the spatial position of the wake boundary from the average PLIF image. Figure 16 shows the wake boundaries for the three Reynolds number conditions at the two different NO seed gas flow rates. This provides further evidence that the NO seed gas does not have a significant impact on the wake shape, as only minor variations are observed (some of these variations may be attributed to the thresholding algorithm of the custom edge-tracking code).

Instantaneous PLIF images that illustrate the various levels of unsteady large-scale structures in the wake flow are shown in Fig. 17 for the three Reynolds numbers. Standard deviation PLIF images, generated as one standard deviation of 100 instantaneous images, are shown in Fig. 18 to further highlight how the unsteady nature of the flow field varies in the wake for the three Reynolds numbers. A similar edge-detection algorithm to the one mentioned earlier was developed and applied to the instantaneous images. The evolution of the upper wake boundary ($r > 0$) for locations downstream of the payload ($z > 0$ mm) is shown in Figure 19 using the instantaneous PLIF data. The mean value of approximately 100 samples are shown as symbols for conditions corresponding to an NO seed gas flow rate of 1 SLM for the three standard Reynolds numbers. The corresponding standard deviation of the upper wake boundary is shown in Fig. 20 to highlight the downstream evolution of unsteady wake boundary.

Time-averaged streamwise velocity vector fields from the molecular tagging velocimetry technique are shown in Figs. 21-23 for the three standard Reynolds numbers. These velocity fields were generated using a custom algorithm that tracked the time-of-flight of the tagged fluorescence lines. For each of the streamwise velocity vector fields shown, the high-speed shear layer, stagnation line, and reverse flow region are clearly seen. Further processing of the MTV data, especially for the test cases with the zoomed-in 100-mm camera lens, is expected to yield instantaneous velocity measurements. This may be used to build statistics to characterize the unsteadiness in the flow field.

Data processing for the additional variations of PLIF, such as the laser frequency scan and temperature imaging, are in progress. Figure 24 shows preliminary results of a custom code that computed the center of the scanned absorption transition using centroids from Gaussian fits, which were obtained by fitting the

$P_1(3.5)$ transition for the $Re_x/L = 0.54 \cdot 10^6$ ft^{-1} test condition. Methods such as the one being developed would be able to provide a measurement of the spanwise velocity and temperature. However, these approaches are challenging, and further processing of the data is required to determine if these approaches are viable for quantitative measurements at these flow (temperature, pressure, velocity) conditions.

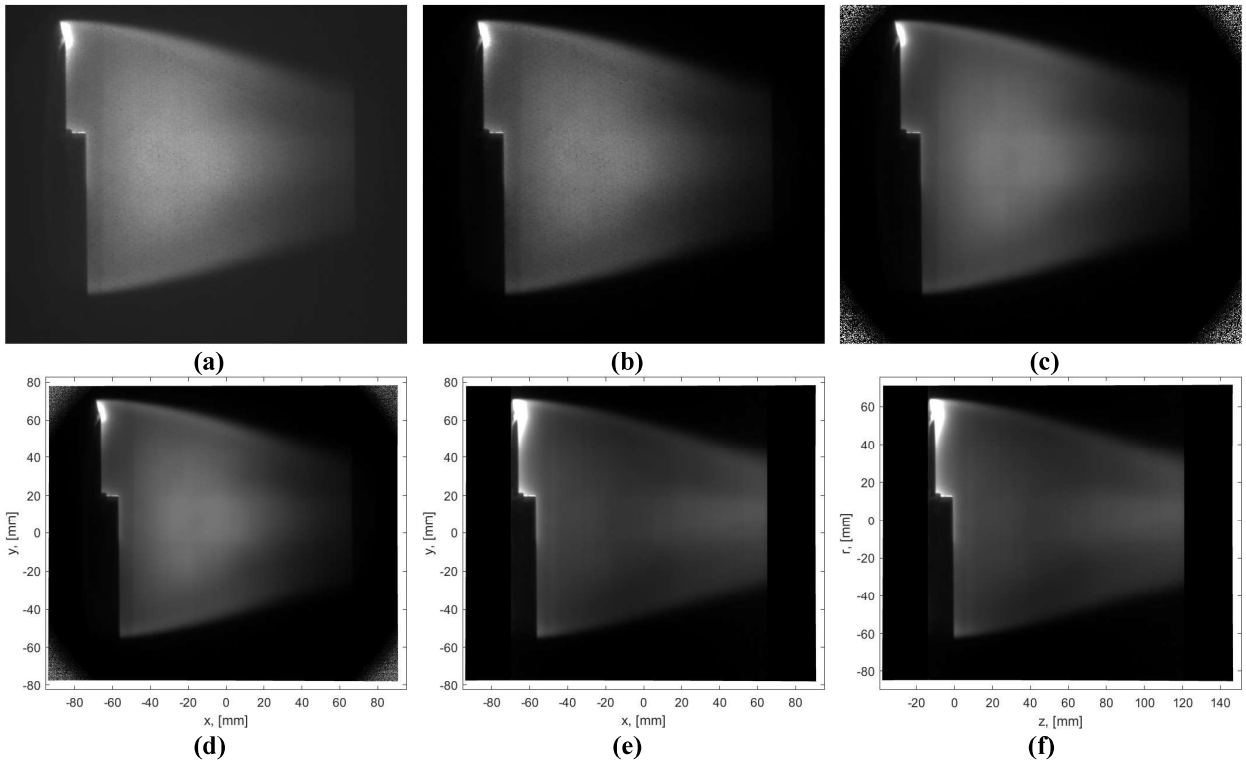

Figure 11. Illustration of the data processing steps for the PLIF flow visualization images: (a) raw image using grayscale, (b) background subtraction, (c) flatfield correction, (d) spatial de-warping and calibration, (e) laser sheet intensity correction, and (f) position of the spatial origin to the model payload.

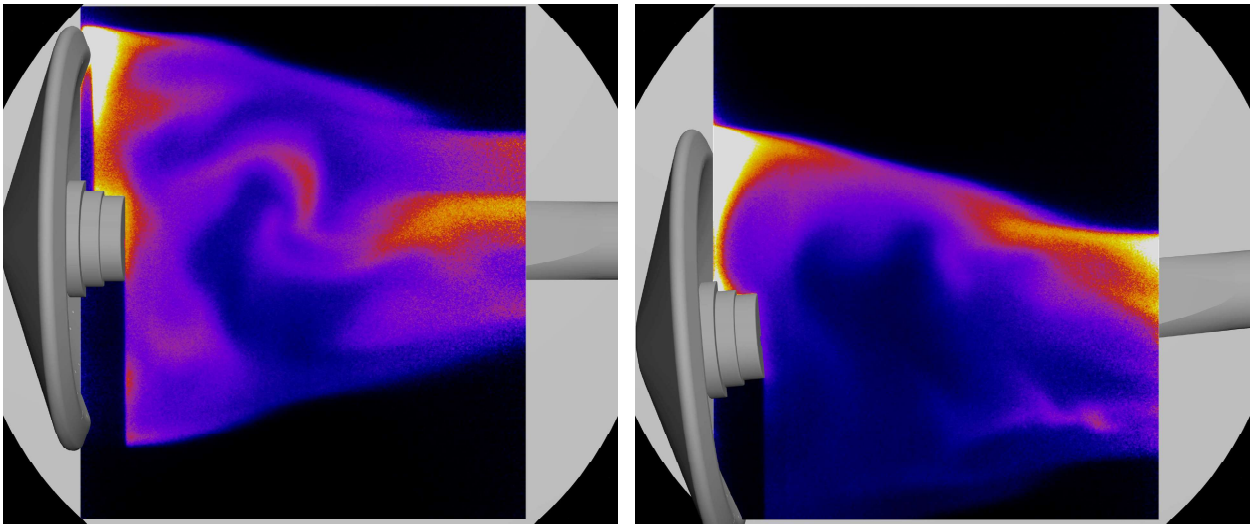

(a) (b)

Figure 12. Rendering of the instantaneous PLIF images for the two model configurations at model roll angle φ = 0°, unit Reynolds number $Re_\infty/L = 0.54 \cdot 10^6$ ft^{-1}, and nitric oxide seed gas flow rate of 1.0 SLM corresponding to two different angle-of-attack: (a) α = 0°, (b) α = -5°.

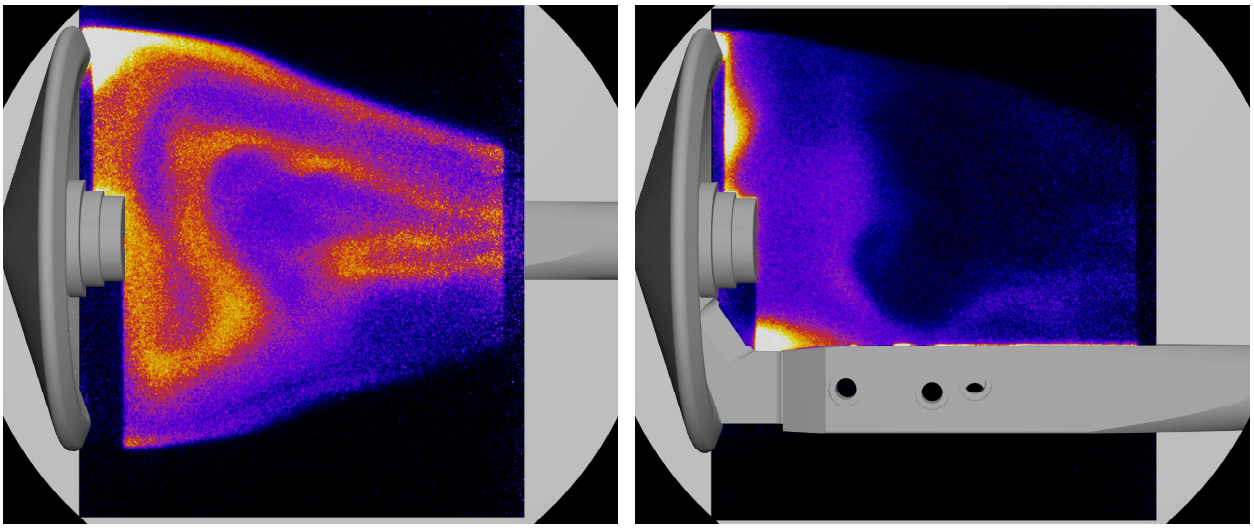

(a) (b)

Figure 13. Rendering of the instantaneous PLIF images for the two model configurations at angle-of-attack α = 0°, unit Reynolds number $Re_\infty/L = 0.54 \cdot 10^6$ ft^{-1}, and nitric oxide seed gas flow rate of 0.05 SLM corresponding to two different model roll angles: (a) φ = 0°, (b) φ = 90°.

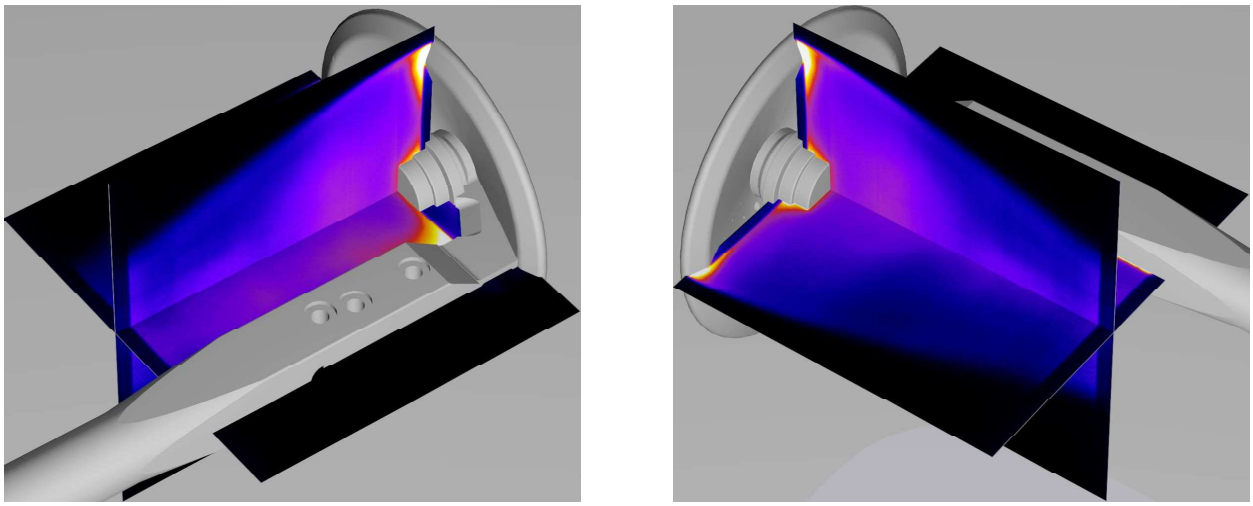

Figure 14. Dual-orthogonal-plane reconstruction of the time averaged average PLIF image oriented with respect to the model, for angle-of-attack α = 0°, unit Reynolds number Re_∞/L = 0.54·10^6 ft^{-1}, and nitric oxide seed gas flow rate of 0.05 SLM. The time averaged PLIF images were generated using 100 instantaneous images for each orientation.

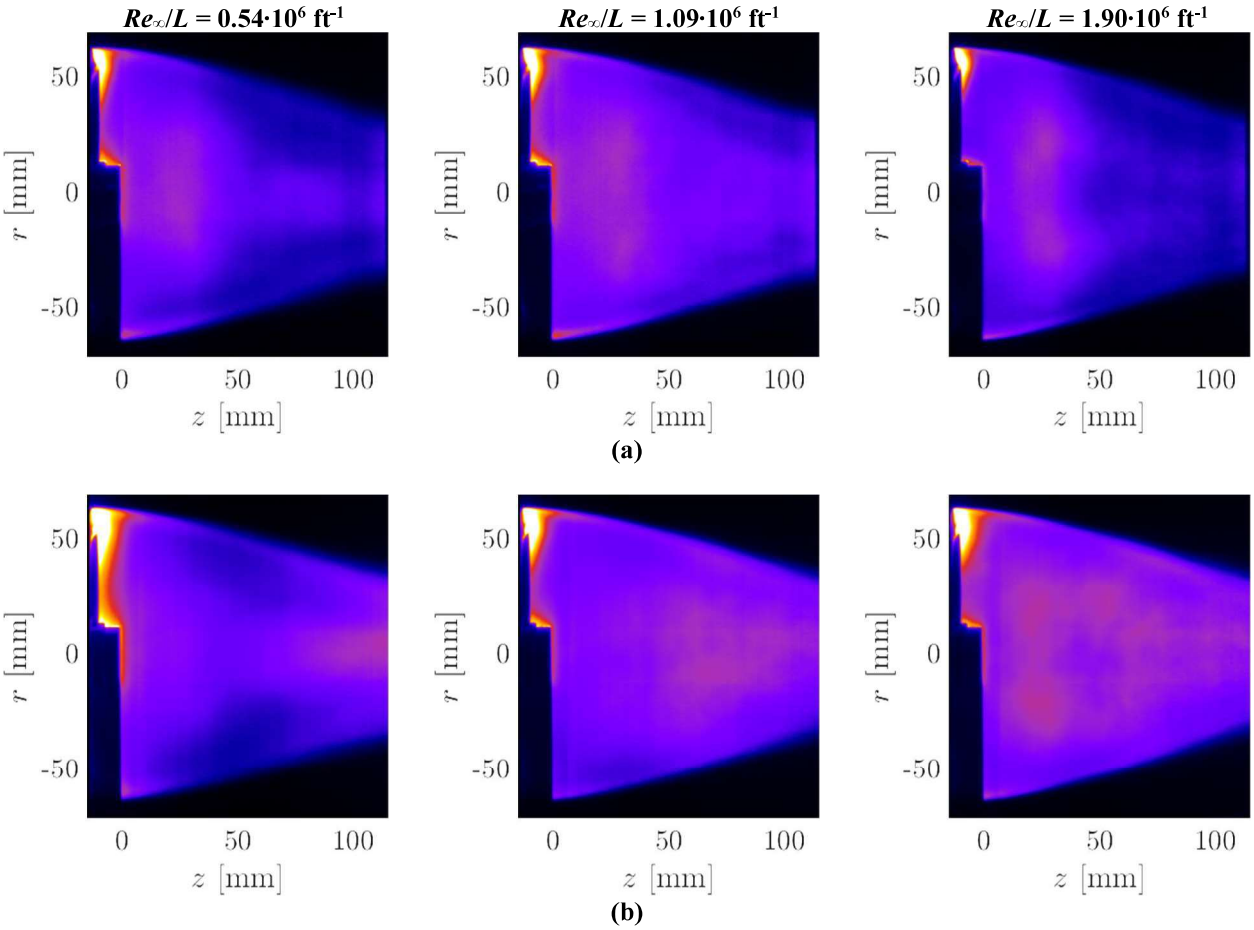

Figure 15. Time averaged PLIF images at the tunnel centerline for three different stagnation pressures corresponding to two different nitric oxide (NO) seed gas flow rates of (a) 0.05 and (b) 1.00 SLM. The time-averaged PLIF images were generated using 100 instantaneous images for each steady-state test condition.

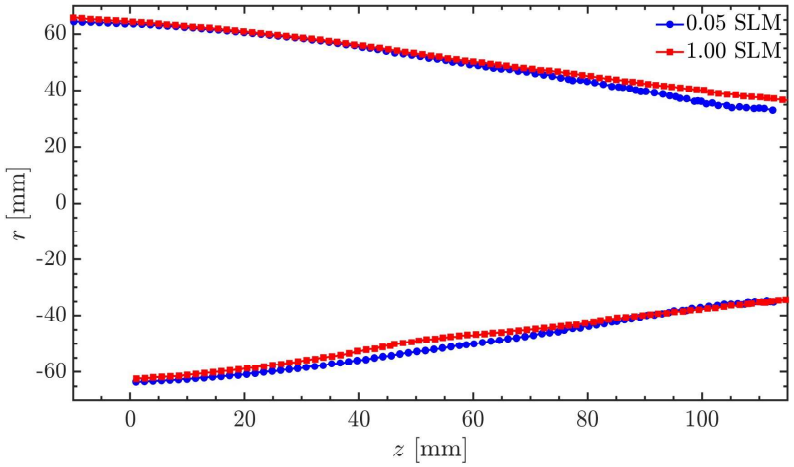

(a)

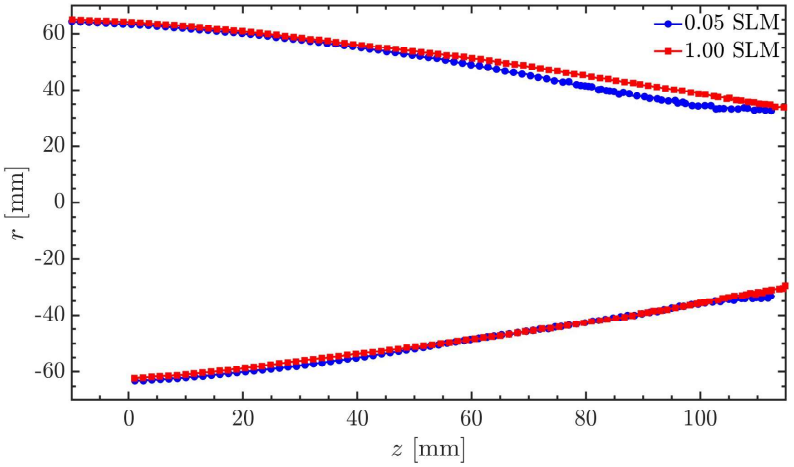

(b)

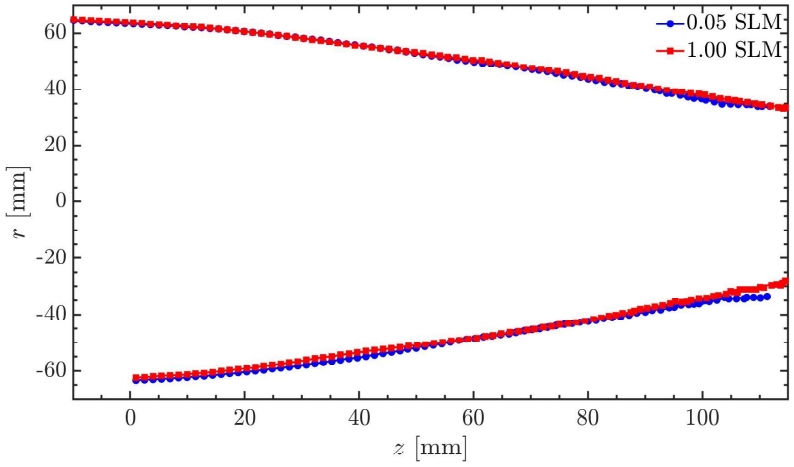

(c)

Figure 16. Wake boundaries based on the time averaged PLIF images, which were generated using 100 instantaneous images for each steady-state test condition, for two different nitric oxide (NO) seed gas flow rates of 0.05 and 1.00 SLM at three different stagnation pressures corresponding to: (a) $Re_\infty/L = 0.54 \cdot 10^6$ ft^{-1}, (b) $Re_\infty/L = 1.09 \cdot 10^6$ ft^{-1}, and (c) $Re_\infty/L = 1.90 \cdot 10^6$ ft^{-1}. One out of every five spatial locations are displayed as symbols for clarity.

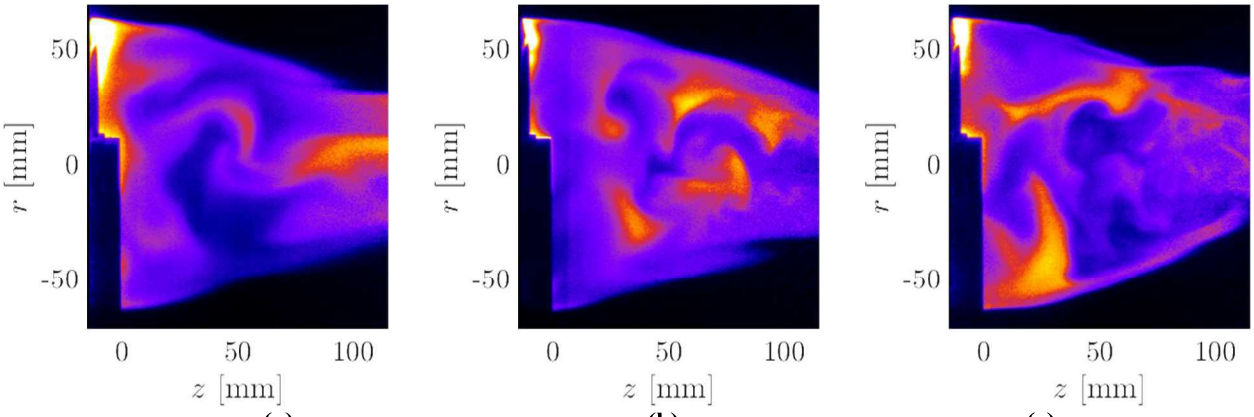

Figure 17. Instantaneous PLIF images for three different stagnation pressures corresponding to: (a) Re_∞/L = $0.54 \cdot 10^6$ ft^{-1}, (b) Re_∞/L = $1.09 \cdot 10^6$ ft^{-1}, and (c) Re_∞/L = $1.90 \cdot 10^6$ ft^{-1}.

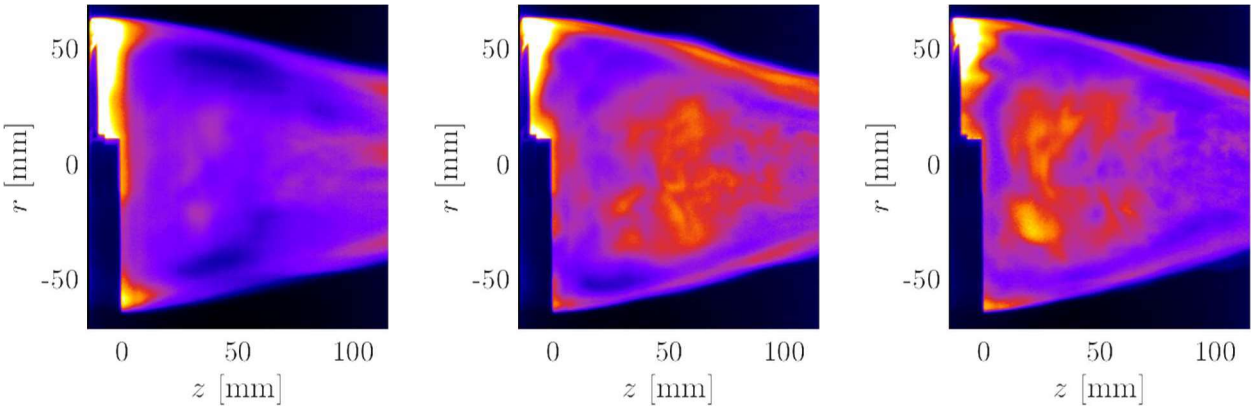

Figure 18. Standard deviation PLIF images for three different stagnation pressures corresponding to: (a) Re_∞/L = $0.54 \cdot 10^6$ ft^{-1}, (b) Re_∞/L = $1.09 \cdot 10^6$ ft^{-1}, and (c) Re_∞/L = $1.90 \cdot 10^6$ ft^{-1}. The standard deviation PLIF images were generated using 100 instantaneous images for each steady-state test condition.

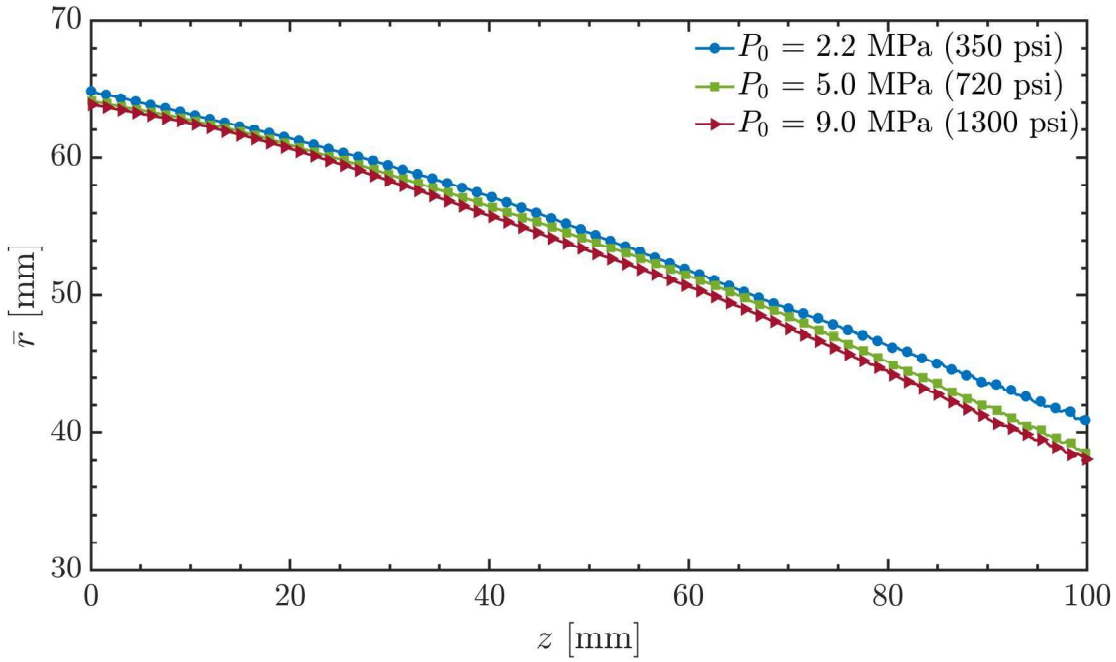

Figure 19. Evolution of the upper wake boundary ($r > 0$) for locations downstream of the payload ($z > 0$ mm) based on the instantaneous PLIF data at a NO seed gas flow rate of 1 SLM for three different stagnation pressures corresponding to $Re_\infty/L = 0.54 \cdot 10^6$ ft^{-1} (2.2 MPa or 350 psi), $Re_\infty/L = 1.09 \cdot 10^6$ ft^{-1} (5.0 MPa or 720 psi), and $Re_\infty/L = 1.90 \cdot 10^6$ ft^{-1} (9.0 MPa or 1300 psi). The mean value of approximately 100 samples are shown, with one out of every ten spatial locations displayed as symbols for clarity.

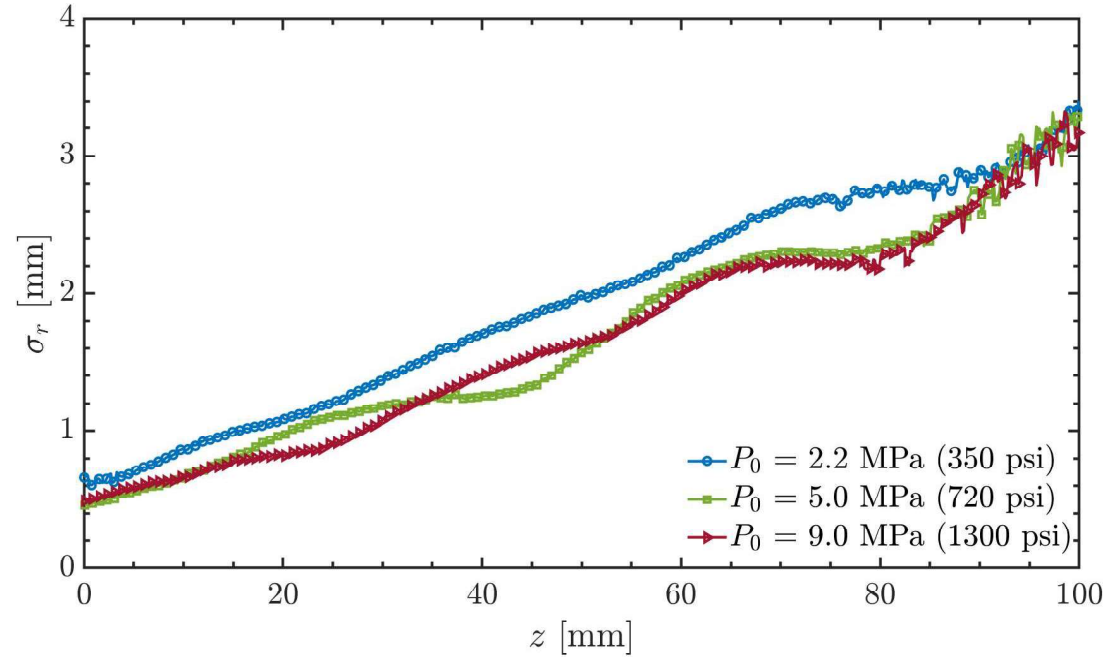

Figure 20. Standard deviation of the upper wake boundary ($r > 0$) for locations downstream of the payload ($z > 0$ mm) based on the instantaneous PLIF data at a NO seed gas flow rate of 1 SLM for three different test conditions corresponding to $Re_\infty/L = 0.54 \cdot 10^6$ ft^{-1} (2.2 MPa or 350 psi), $Re_\infty/L = 1.09 \cdot 10^6$ ft^{-1} (5.0 MPa or 720 psi), and $Re_\infty/L = 1.90 \cdot 10^6$ ft^{-1} (9.0 MPa or 1300 psi). Approximately 100 samples are used for each location, with one out of every five spatial locations displayed as symbols for clarity.

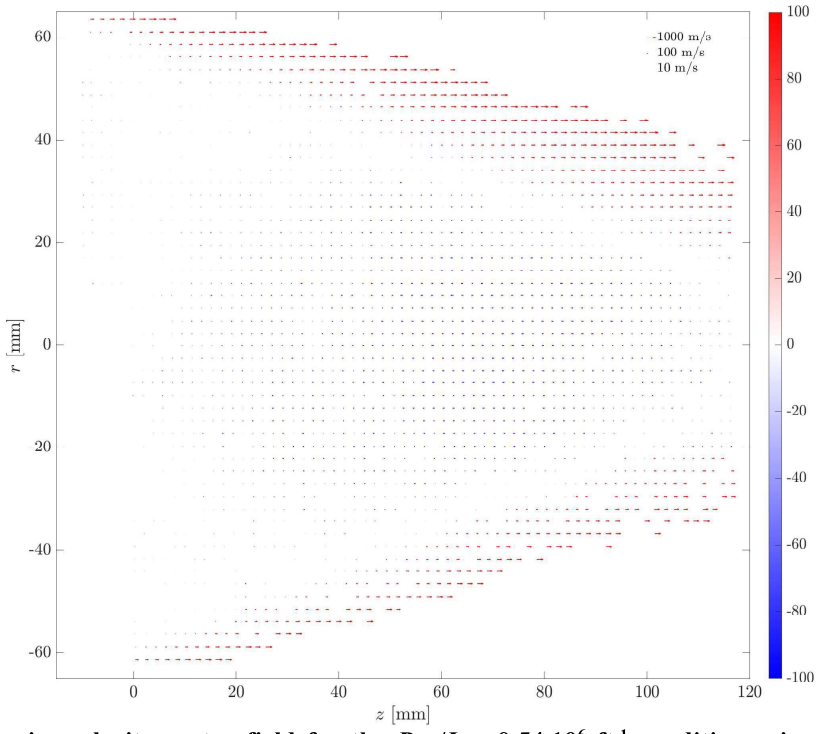

Figure 21. Streamwise velocity vector field for the Re_τ/L = 0.54·10^6 ft^{-1} condition using molecular tagging velocimetry (MTV) showing the vector field with a linear scale and color bar scaled to ± 100 m/s to highlight streamwise velocity stagnation regions.

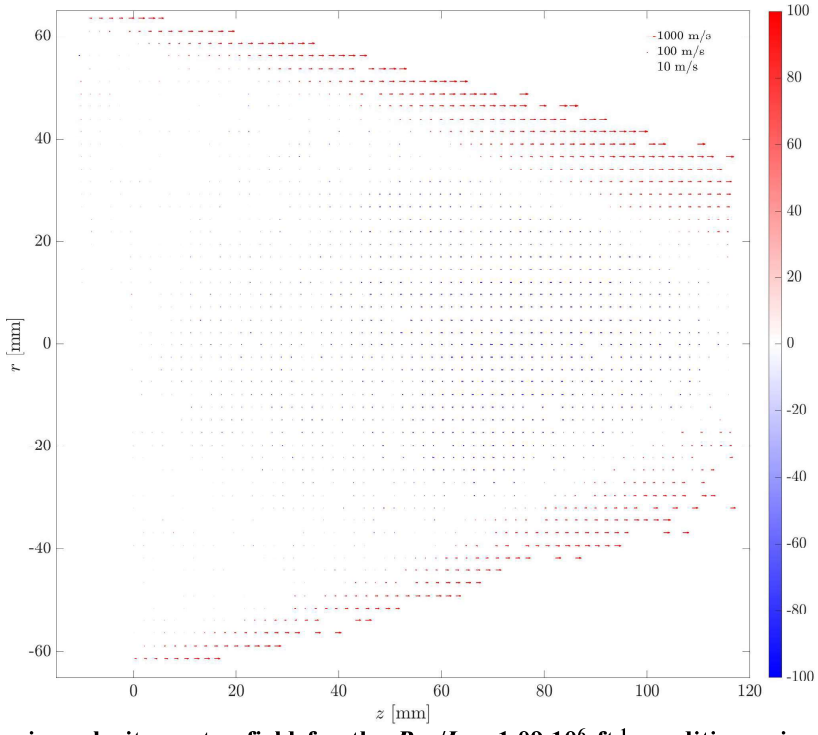

Figure 22. Streamwise velocity vector field for the Re_τ/L = 1.09·10^6 ft^{-1} condition using molecular tagging velocimetry (MTV) showing the vector field with a linear scale and color bar scaled to ± 100 m/s to highlight streamwise velocity stagnation regions.

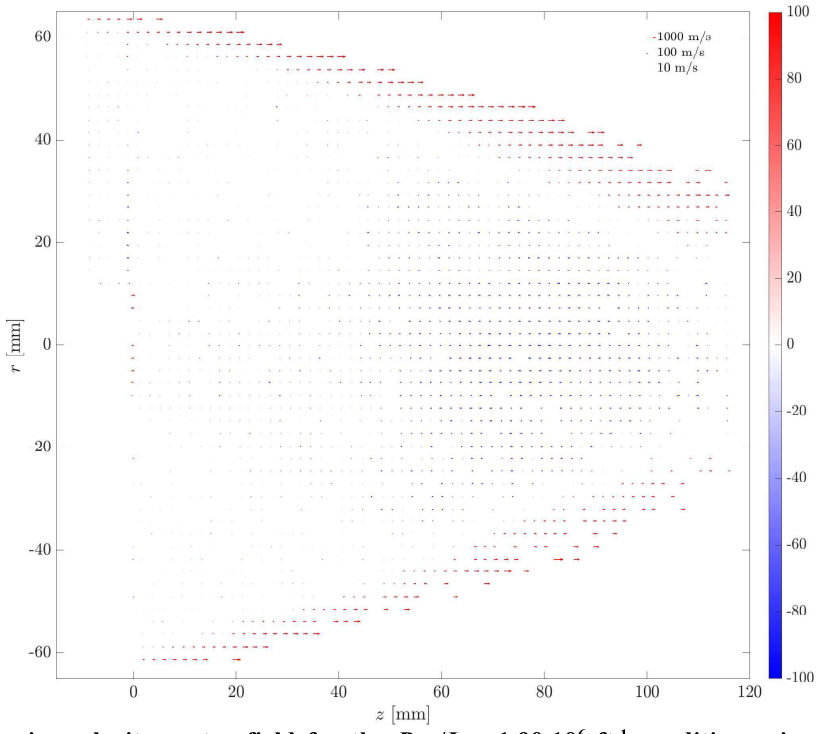

Figure 23. Streamwise velocity vector field for the Re_∞/L = 1.90·10^6 ft^{-1} condition using molecular tagging velocimetry (MTV) showing the vector field with a linear scale and color bar scaled to ± 100 m/s to highlight streamwise velocity stagnation regions.

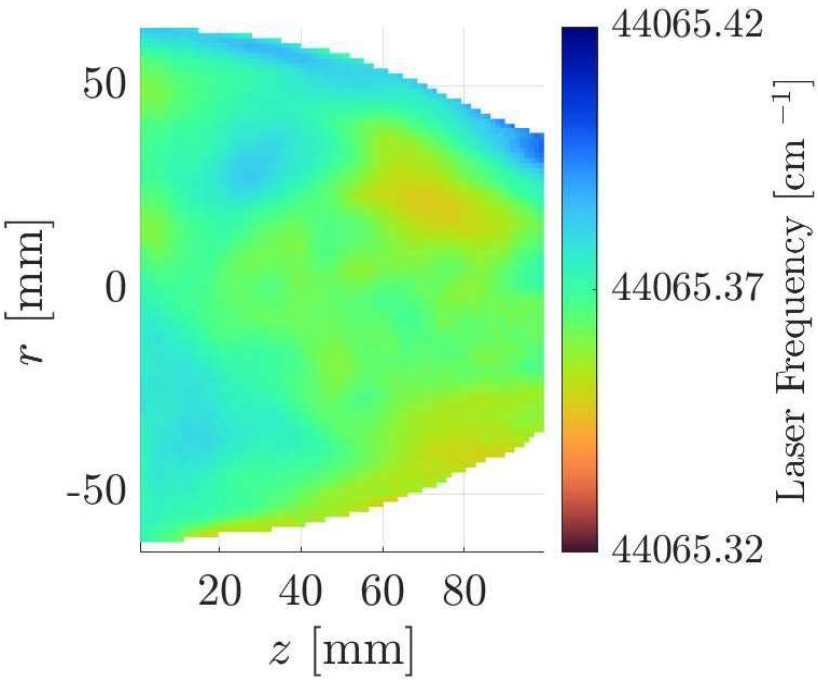

Figure 24. Computed center of the absorption transition using centroids from Gaussian fits obtained by fitting the P$_1$(3.5) transition for the Re_∞/L = 0.54·10^6 ft^{-1} test condition.

Summary

This report documents an experimental dataset of hypersonic wake flow measurements obtained at the NASA Langley 31-in Mach 10 Tunnel. The planar laser-induced fluorescence (PLIF) technique was used to obtain off-body measurements of a blunt body model based on the aeroshell used for the LOFTID flight vehicle (Swanson, *et al.*, 2019). The experimental test conditions from the measurement campaign are documented and an initial analysis of select test conditions are provided. PLIF flow visualization was performed while varying parameters such as the NO flowrate, angle of attack, roll angle, and the freestream Reynolds numbers. Velocity measurements using molecular tagging velocimetry (MTV) were also successfully attained during the test campaign. Some additional measurements were also acquired to explore other potential measurement techniques based on variations of the PLIF method.

References

Bathel BF, Danehy PM, Inman JA, Jones SB, Ivey CB, Goyne CP, "Velocity Profile Measurements in Hypersonic Flows Using Sequentially Imaged Fluorescence-Based Molecular Tagging", AIAA Journal 49(9), 2011.

Berger K, Rufer S, Hollingsworth K, Wright S, "NASA Langley Aerothermodynamics Laboratory: Hypersonic Testing Capabilities, *53rd AIAA Aerospace Sciences Meeting*, 2015.

Cagle CM, "LOFTID Wake Flow Model", *MSR 1299750*, 2021.

Danehy PM, Weisberger J, Johansen C, Reese D, Fahringer T, Parziale NJ, Dedic C, Estevadeordal, Cruden BA, "Non-Intrusive Measurement Techniques for Flow Characterization of Hypersonic Wind Tunnels", *NATO STO Manuscript on Hypersonic Freestream Characterization*, 2018.

Eckbreth A C, "*Laser Diagnostics for Combustion Temperature and Species"*, 2nd ed., Overseas Publishers Association, Amsterdam, 1996.

Swanson GT, Kazemba CD, Hughes CD, Johnson RK, Lindell MC, Bodkin RJ, DiNonno, Cheatwood FM, "LOFTID Aeroshell Engineering Development Unit Structural Testing", *International Planetary Probe Workshop*, 2019.

Schwartz RJ and Fleming GA, "Virtual Diagnostics Interface: Real Time Comparison of Experimental Data and CFD Predictions for a NASA Ares I-Like Vehicle," *22nd International Congress on Instrumentation in Aerospace Simulation Facilities*, 2007.